Quantifying melt dynamics on a debris-covered Himalayan glacier using repeated UAS photogrammetry derived DSM and point cloud differencing

Niti B. Mishra[1*], Gargi Chaudhuri[1], Kumar P. Mainali[2,3], Suraj Mal[4], Paras B Singh[5] and Babulal Tiruwa[5]

[1]*Department of Geography & Earth Science, University of Wisconsin-La Crosse, WI 54601, USA*

[2] *Department of Biology, University of Maryland, 1210 Biology-Psychology Bldg, College Park, MD, 20742–4415, USA*

[3]*Conservation Innovation Center, Chesapeake Conservancy, Annapolis, MD 21401, USA*

[4]*Department of Geography, Shaheed Bhagat Singh College, University of Delhi, New Delhi 110017, India*

[5]*National Trust for Nature Conservation (NTNC), P.O. Box 3712, Khumaltar, Lalitpur, Nepal*

Abstract

Debris-covered glaciers are a notable feature in the greater Himalaya, and their ongoing mass loss under changing climate will affect the water resources of over a billion people. The current knowledge of the mass balance of Himalayan glaciers is restricted by the paucity of in-situ measurements of glaciers in both space and time, as well as the resolution of satellite remote sensing imageries. Recently, the use of Unmanned Aerial System (UAS) imagery has shown the potential to bridge this gap by enabling very detailed monitoring of inaccessible glacial areas. UAS imagery-based monitoring of Himalayan glaciers has so far been limited to a single glacier in the entire Himalaya, providing a limited understanding of spatial variability in glacier mass balance and driving factors. In the first UAS based glacial mass change estimation in the trans-Himalaya, we conducted two Unmanned Aerial System (UAS) surveys (May and November 2019) over the debris-covered Annapurna III glacier in the Himalaya. We performed Structure-from-Motion (SfM) analysis and utilized differential GPS field observations to derive geometrically accurate point clouds, ortho-mosaics and digital surface models (DSMs). The glacial volumetric loss was estimated from DSM differencing, and the magnitude and spatial variability of glacier surface change was derived from 3-D differencing of point clouds. Results revealed a heterogeneous glacial melt pattern, with an average elevation loss of 0.89 m during the monitored time period. The majority of the glacial tongue exhibited surface lowering except the area above and around the glacial snout that surprisingly exhibited significant elevation gain. Both the highest magnitude of mass loss and the highest spatial variability in mass change was observed in areas with exposed ice-cliffs and supraglacial ponds. Glacial surface velocity derived from manual feature tracking showed velocity ranging from 0-4.1 m. A detailed evaluation of specific areas allowed an improved understanding of the complex interplay of factors leading to observed surface change. Our findings expand the extent of UAS based monitoring of debris-covered glaciers in the Himalaya and conclude that UAS derived 3D topographic products will become increasingly important for monitoring of thinning debris-covered glaciers.

Keywords: UAS, debris-covered glacier, trans-Himalaya, aerial photogrammetry, structure from motion, DSM differencing, point cloud differencing, glacial mass balance, ice-cliffs

*Corresponding author email: *nmishra@uwlax.edu*

1. Introduction

Valley glaciers, particularly in tropical and sub-tropical latitudes are recognized as a strong indicator of climatic change due to their sensitivity to small changes in climatic variables (Kaltenborn et al., 2010; Oerlemans, 2001). The High Asian mountain systems, including Hindukush, Karakoram and Himalaya holds the largest volume of glaciers outside polar areas (Farinotti et al., 2019). Himalayan glaciers are significant source of meltwater (Kehrwald et al., 2008) and therefore changes in their area, volume and melt regime will significantly alter downstream hydrology and water supply to ~1.8 billion population in ten major Himalayan river catchments (Immerzeel et al., 2012; Immerzeel et al., 2010). These changes could have a profound effect on the human livelihood and ecology in many countries in South Asia (Kaltenborn et al., 2010; Mishra and Mainali, 2017; Schickhoff and Mal, 2020; Shrestha and Aryal, 2011; Xu et al., 2009). Being in one of the most rapidly warming region of the world, the Himalayan glaciers are important to study both for the enormous socio-economic aspect of climate change impact as well as scientific understanding of the dynamics of glacier response itself. Large scale monitoring of changes in key glacial parameters in the Himalaya (e.g. glacial area, mass balance and surface velocity) is therefore critical for understanding how climatic change impacts glaciers (Cogley, 2011) and in formulating informed decisions and policies (Bhadwal et al., 2013; Sud et al., 2015).

Methodological developments in monitoring glaciers has seen substantial changes in the past few decades. The traditional field-based methods for glacial mass balance and surface velocity estimation (e.g. by monitoring ablation stakes and accumulation pits) can provide an accurate measurement of glacial dynamics at a local scale (Hubbard and Glasser, 2005). However, field methods are limited in scope and extent due to glacier inaccessibility, time requirement and prohibitive expenses associated with field expeditions. Additionally, many Himalayan glacier have thick debris-cover, which makes installation and maintaining instruments cumbersome (Dobhal et al., 2013). More recent methodological developments, which includes use of space and air-borne multi-temporal remotely sensed datasets, have complimented field-based glaciological measurements making it possible to routinely monitor changes in the glacial extent, mass balance and derive surface velocity vectors over large swaths of the cryosphere in a more time efficient and relatively inexpensive manner (Bishop et al., 2004; Paul et al., 2015).

Deriving changes in glacier surface elevation with elevation models and glacier surface velocities has been achieved using both active (Kääb et al., 2012) as well as passive satellite sensors (Bolch et al., 2011; Paul et al., 2015). Although satellite remote sensing enables monitoring large areas, the resolution of derived products is relatively coarse (> 30 m), and the vertical error range is high (> 15 m) (Fujita et al., 2008). Fine-scale spatial patterns of mass balance and surface velocity in Himalayan glaciers is regulated by geomorphic properties such as debris cover and sub-glacial bedrock slope gradients. Debris cover arguably provides an insulation effect. Studies have found that debris-covered glaciers experience lower glacial down-wasting rate compared to non-debris-covered area (Scherler et al., 2011). However, more recent studies have found that debris-covered areas showed the same rate of mass loss as debris free area (Kääb et al., 2012; Pellicciotti et al., 2015).

To understand the role of variable debris cover thickness and englacial features (ice-cliffs, supraglacial ponds) on spatial patterns of melting and mass loss, studies have emphasized the need for finer scale monitoring (i.e. pixel size < 0.5 m) of glaciers for which satellite data showed limited potential (Kirschbaum et al., 2019). More recently, the application of imagery acquired using Unmanned Aerial System (UAS) has enabled monitoring of the rapidly changing glacial geomorphic features at finer spatial scales. UAS has the ability to be rapidly deployed for data collection, provides the flexibility to perform repeated surveys and generally provides much finer resolution data (< 0.1 m) (Bhardwaj et al., 2016; Mishra et al., 2018). UAS derived topographic models have been utilized to study fine-scale glacial changes in various mountain systems including in the Coriallera Blanca (Wigmore and Mark, 2017), Alps (Rossini et al., 2018), and in the Himalayas (Immerzeel et al., 2014).

Multi-temporal Digital Surface Models (DSMs) derived from UAS have been used to perform DSM differencing to detect and quantifying highly heterogeneous patterns of ice loss (Immerzeel et al., 2014) and have shown how ice-cliffs influences the spatial patterns of mass loss on debris-covered glacier (Immerzeel et al., 2014; Ragettli et al., 2016). DSM differencing has been widely used for quantifying 3D topographic change; however recent studies have reported low accuracy and higher uncertainty. Transforming data into DSM requires gridding or meshing, leading to poor representation of steep slope or steep sloping topography (James et al., 2017). Several of these challenges associated with DSMs are addressed by computing three-dimensional change directly on pair of point clouds (Smith et al., 2016). Point cloud differencing is better suited for quantifying statistically significant change in glaciers with ice-cliffs and other supraglacial features were the geometry changes in 3D (Brun et al., 2016; Watson et al., 2017). While few studies that perform direct comparisons of multi-temporal point clouds for glacier scale analysis have been undertaken in the Alps (Rossini et al., 2018), they are yet be extensively tested on Himalayan glaciers.

The only glacier that has so far been studied using UAS data in the Himalaya is the Lirung glacier which lies on the southern slope of Himalaya and falls under the monsoonal climatic regime. To the best of our knowledge, UAS based changes in glacial mass balance have not been studied on the north-facing slopes in the Himalayas, which typically have drier climatic regime since it falls in the trans-Himalayan zone outside the monsoonal climatic regime. Our efforts expand the use of UAS to investigate a trans-Himalayan glacier. While Lirung glacier has been studied using fixed-wing UAS, here we use a quadcopter UAS. For this study, we performed repeat UAS surveys combined with dGPS measurements at Annapurna III glacier in the trans-Himalayan Manang valley, Nepal. The objectives are (i) to quantify changes in ice melt, glacier volume and glacier surface velocity at very fine scale with high accuracy (ii) to compare the spatial variation of observation changes over the monitored area and (iii) to investigate finer-scale processes and patterns of glacier changes to understand the role of local topography and geomorphological features in controlling the spatial variability in changes in glacial mass.

2. Materials and methods

2.1 Study area

The Annapurna III glacier (locally known as Syakung) is located on the northern slopes of the Annapurna range in the Manang district of the Nepalese Himalaya (28.628466°N , 84.040127°E) (Figure 1). Although the glacier is part of the Annapurna massif but it lies in the trans-Himalaya outside the monsoon regime and receives very little monsoonal precipitation. The climate is characterized as dry with annual rainfall totaling 398 mm, most of which occurs in summer months (June-Sept) (Kansakar et al., 2004). The glacier tongue is detached from the steep accumulation slopes below Annapurna III peak (7555m) and is fed by avalanches and seasonal snowfall during winter months. Like other Himalayan glaciers, Annapurna III glacier has a debris-covered tongue and the glacier snout is located at an elevation of 3848 m above mean sea level.

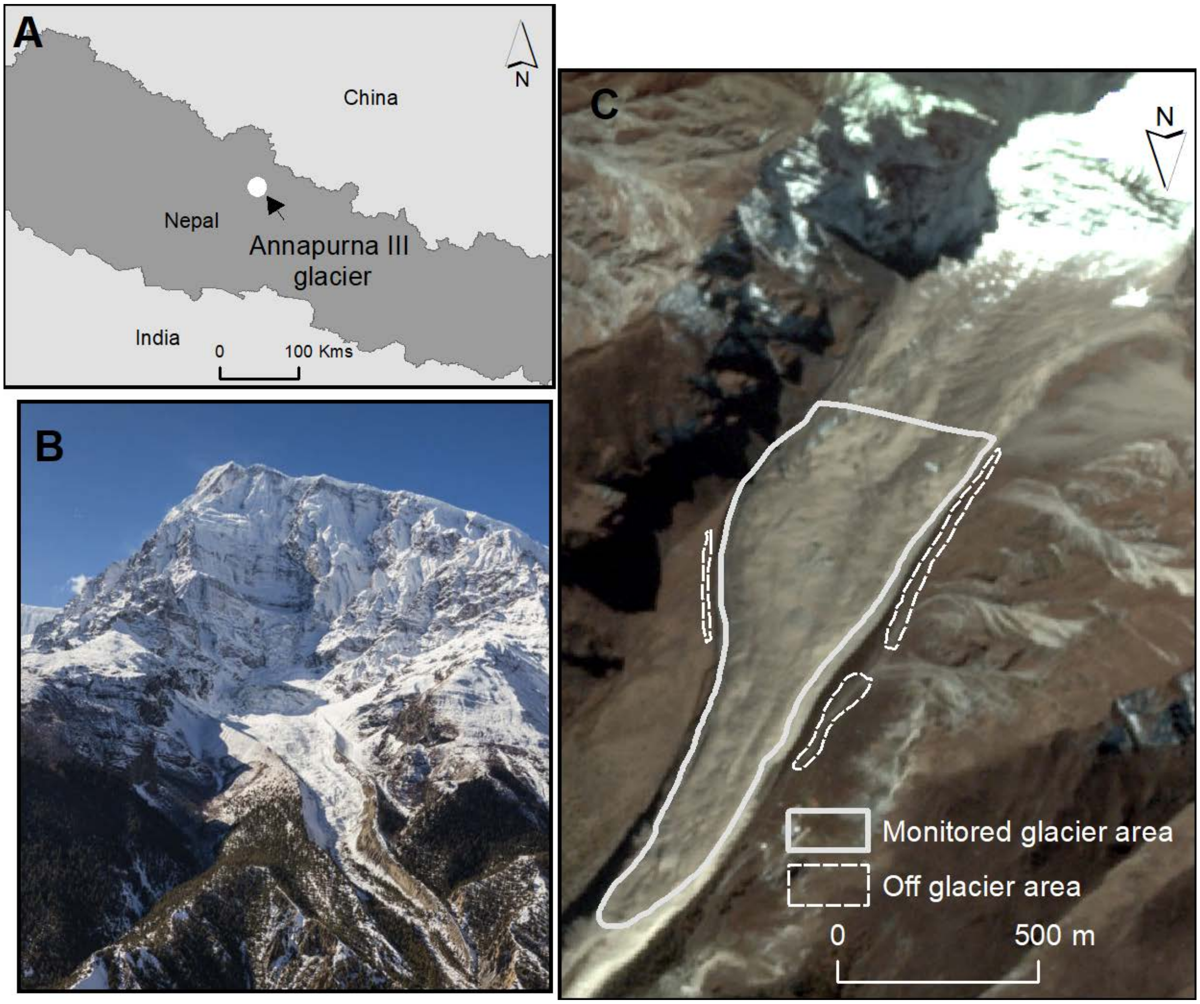

Figure 1: (A) Position of Annapurna III glacier in Nepal Himalaya, (B) an on-the ground view of the Annapurna III glacier from the opposite aspect showing the accumulation zone transitioning to ablation zone and (C) the monitored glacier area and the off-glacier area used for accessing accuracy. The background is a PlanetScope imagery of October 11, 2019

2.2 Unmanned aerial system surveys

Annapurna III glacier was surveyed by UAS twice, first on May 16-17, 2019 and later on November 20-21, 2019. This time-frame represents the starting and the end of glacial ablation season. Images were collected using a rotary-wing UAS (Mavic 2 pro from DJI) fitted with a GPS/GNSS satellite positioning system and a 20 Megapixel Hasselblad camera (i.e. 5472 by 3648 pixels) that capture JPEG format images (Figure 3.c) (DJI, 2019). (Table 1).

Table 1: UAS and camera specification

UAS and sensor Specifications	
Dimensions	Unfolded: 322×242×84 mm (length×width×height)
Max Flight Time (no wind)	31 minutes (at a consistent 25 kph)
Max Flight Distance (no wind)	18 km (at a consistent 50 kph)
Max Wind Speed Resistance	29–38 kph
Operating Temperature Range	-10°C to 40°C
Takeoff Weight	907 g
Storage	8 GB (Internal), External Micro SD™
Global Navigation Satellite	GPS+GLONASS
Sensor	1” CMOS
Lens	FOV: about 77°, 35 mm Format Equivalent: 28 mm Aperture: f/2.8–f/11, Shooting Range: 1 m to ∞
ISO range	Photo:100-3200 (auto)
Shutter Speed	Electronic Shutter: 8–1/8000s
Image Resolution	5472×3648

Map Pilot for DJI app was used to pre-program mission parameters which were uploaded to the UAS autopilot to fly a grid pattern at a constant elevation (with respect to ground) (Easy, 2017). The Map Pilot for DJI app was used to calculate the area and estimate how many batteries/flights were needed to acquire images over the entire study area. The app features an interface for mission plan, allowing for setting parameters such as distance, a maximum speed of aircraft, waypoint altitude, resolution, and duration time for flight planning and a connected display for aircraft. As the study area had a variable altitude (from approximately 3750 to 4350 m), the UAS was programmed to adapt its flight altitude to maintain a constant height above the glacier surface (defined using the “terrain follow” feature in the Map Pilot app which uses a 30 m ASTER GDEM2 to derive changes in altitude for flight) (Easy, 2017)(Figure 2).

Figure 2: Flight parameters used for UAS missions within the Map Pilot for DJI app

The imagery acquisition was performed in 22 separate flights, 9 of which were conducted in May 2019 and the remaining 13 flights in November 2019 (Table 2). Due to a functioning battery recharging facility in November 2019, a higher number of flights could be conducted and as a result, higher elevation reaches of the glacier that could not be mapped in May 2019 expedition were mapped in November 2019 (Figure 4). For all flights average flight altitude was set to 90 m above ground, a forward image overlap was set to 80% and sidelap was set to 75%, and flight speed was set to 4 m/second (Figure 2).

Table 2: Overview of UAS survey conducted in May and November 2019

	Total # of flights	Total # of images captured	# of images used	Area mapped	Flying altitude	GSD (spatial resolution)
May 16 -17, 2019	9	2101	2081	0.62 km^2	90 m	2.1 cm/pixel
Nov 20 -21, 2019	13	3042	3026	1.197 km^2	90 m	2.1 cm/pixel

2.3 Ground control points

In May 2019, before the UAS data collection, 27 ground control points (GCPs) were established and surveyed using a differential GPS setup (Figure 3 and Figure 4). These GCPs were strategically placed along the lateral moraines of the Annapurna III glacier. The GCPs were created using white or red color painted circular targets on sufficiently large and stable rocks and were utilized for georectification of the photogrammetric point cloud and as check points for accuracy assessment (Figure 3.b). In November 2019, 4 more GCPs were added in the higher elevation reached along the western moraine of the glacier. The targets were distributed fairly evenly across the mapped area. However, reaching the higher elevation of the study area (with nearly vertical slopes and ice-fall) was extremely difficult and targets could not be established there (Figure 4).

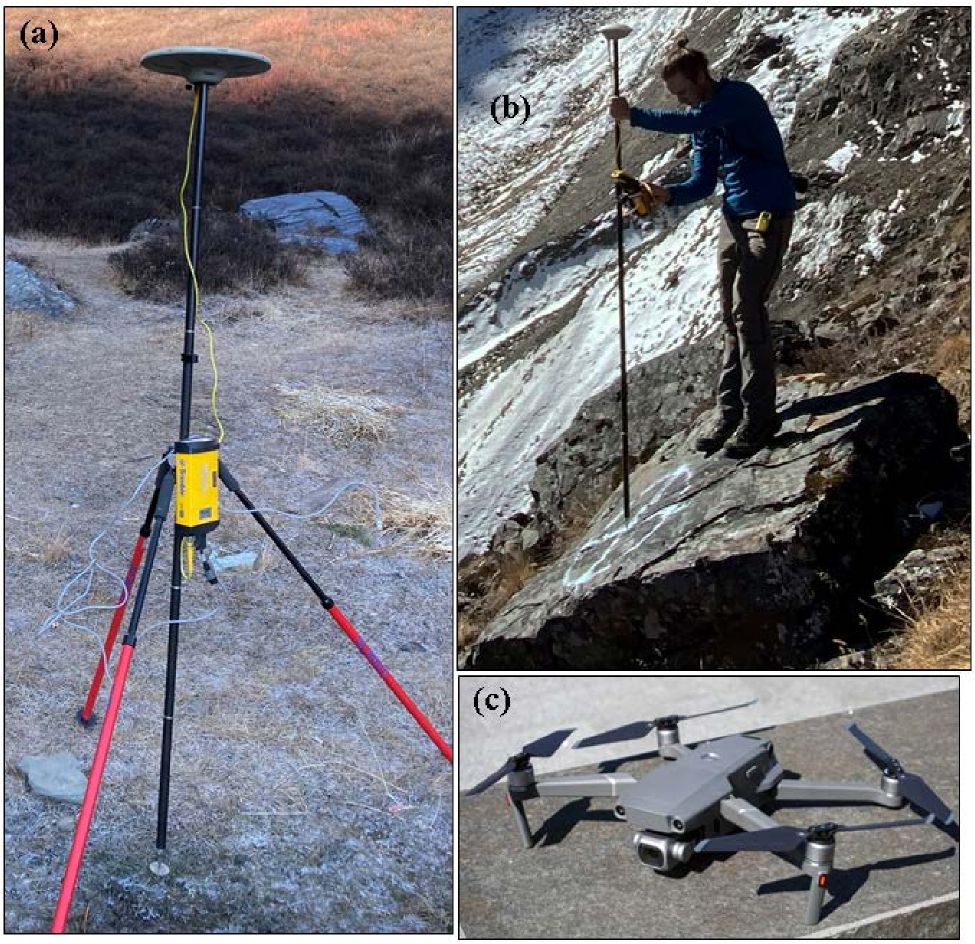

Figure 3: (a) A differential GNSS base station setup near the Annapurna-III glacier (location shown in figure 4), (b) the GNNS rover collecting data over a marked Ground Control Point (GCP) and (c) the quadcopter AS utilized for data collection over the study area.

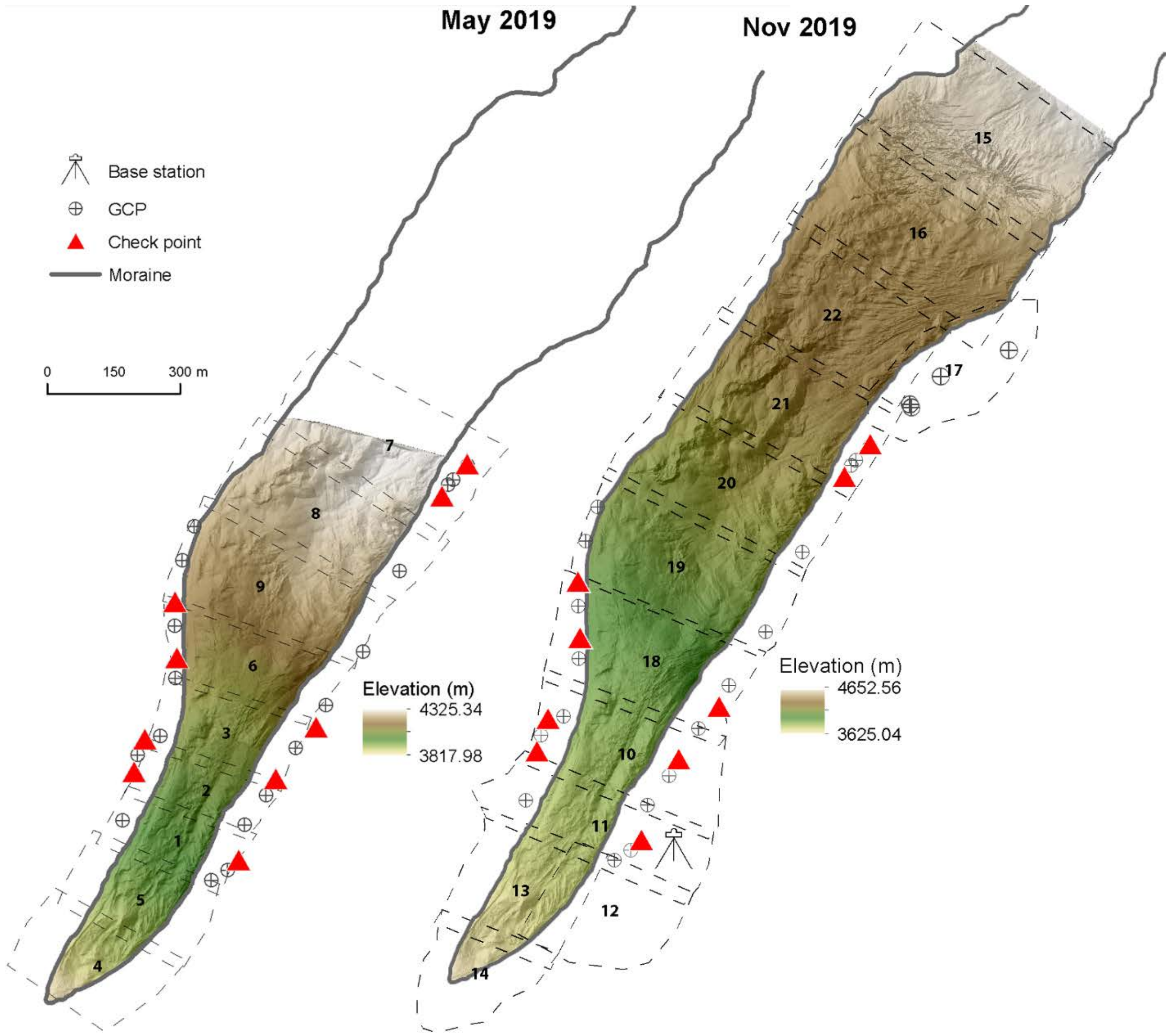

Figure 4: Overview of the imaged area using UAS, check points and ground control point locations for May 2019 and Nov 2019 survey missions for Annapurna III glacier.

Two differential GPS devices, a base station and a rover were utilized. A Trimble Net R5 base with Zypher Geodetic antenna was installed on a tripod near the western lateral moraine in proximity to the camping site (Figure 3.a). The base station was set up to collect data every 10-second for a 15 hour period (i.e. entire duration of the rover data collection). Two Trimble GeoXH 6000 units were used as rovers (Figure 3.b). To avoid error due to changes in antenna pole inclination, the GCPs were recorded every second for a duration of 1-minute. These datasets were later post-processed with Trimble Pathfinder office software (Trimble, 2000).

2.4 SfM processing-Point cloud, DSM and Ortho-mosaic generation

The images collected during May and November were analyzed to generate 3-D point clouds and 2-D otho-mosiacs of the Annapurna III glacier and surrounding area following SfM workflows (Lucieer et al., 2014). We performed SfM analysis in Pix4Dmapper Pro software (Switzerland, 2018). Specific detailed of algorithms implemented in Pix4D package are not available due to the proprietary nature of the software but some details regarding the parameters utilized within the software can be found in (Pix4D, 2019). The first step of SfM processing starts by selecting quality photos with sufficient overlap from multiple angles and positions. These high quality photos are aligned using an scale invariant feature recognition method (Lowe, 1999) to find and match unique image features (called 'key points') that are stable and are found in relation to their neighboring pixels. In the following step, a bundle block adjustment is made on the matched features to generate a sparse 3D point cloud (Snavely et al., 2008; Triggs et al., 1999). The GCPs were manually identified facilitated by this sparse point cloud whereby the dGNSS coordinates of each GCP was manually imported and precisely marked in multiple corresponding images to improve the accuracy of the 3D point cloud. Finally a densification technique is applied using multi-view stereo (MVS) to increase the density of the point cloud (approximately 102,000,000 and 183,000,000 points respectively for May and November 2019) (Table 3) and also produce Digital Surface Models (DSMs) and ortho-mosaics.

Table 3: Estimated pixel matching and model construction errors from SfM processing workflow.

	May 2019	Nov 2019
2D keypoints for bundle adjustment	26,723,614	43,438,291
3D keypoints for bundle adjustment	9,217,775	14,971662
Mean reprojection error	0.134	0.140
Mean GCP *X* error/sigma RMSE	-0.003758 m ± 0.028974 m 0.029216 m	0.000149 m ± 0.012517 m 0.012518 m
Mean GCP *Y* error/sigma RMSE	0.006088 m ± 0.029652 m 0.030270 m	0.000611 m ± 0.008463 m 0.008485 m
Mean GCP *Z* error/sigma RMSE	-0.024147 m ± 0.066237 m 0.070502 m	-0.000719 m ± 0.015976 m 0.015992 m
Maximum DSM resolution	0.0217 m	0.0212 m
Average Point cloud density	274 per m^3	298 per m^3

2.5 Accuracy assessment

The accuracy of the DSMs were accessed in multiple ways. Firstly, the SfM processing provided horizontal and vertical residuals (i.e. the differences between actual and estimated coordinates during the bundle adjustment and model generation process) for the 18 GCPs used in the two surveys (Table 3). Error is provided as mean and sigma of x-y-z differences, which describes how well the point cloud fits the in-scene ground targets. Secondly, the horizontal and vertical residuals calculated by overlaying 9 independent validation check points and comparing them against the x-y-z values extracted from DSM surface provide a more unbiased and precise error estimate. Additionally, the vertical uncertainty was also evaluated by calculating differences between the May and November DSMs for off-glacier terrain areas that were not subject to any change during the study period.

2.6 *Tracking of glacier surface velocity*

After confirming the precise geo-registration of the May and November 2D and 3D model outputs, glacial dynamics during the study period were examined using multiple approaches. The surface velocity and displacement of the glacier between May and November 2019 was estimated following a manual feature tracking method similar to Immerzeel et. al (2014). A total of 93 clearly distinguishable surface features points were digitized on the ortho-mosaic and their horizontal displacement between the two dates were precisely measured. The resulting velocity vectors at point locations were interpolated using ordinary kriging method to create a continuous surface.

2.7 Comparison between May and November DSMs and point clouds

To be able to make accurate comparisons for deriving melt water patterns and changes in volume across the glacier, it was necessary to remove any horizontal moment before comparison. For this purpose, the direction and magnitude of the vectors derived above were utilized to orthorectify the November 2019 DSM to exactly match the May 2019 DSM. The two DSMs were clipped to an interpreted glacial boundary. Furthermore, to reduce the probability of any spatial mismatch, the DSMs were resampled to 0.1 m pixel resolution and then the May DSM was subtracted from the November DSM to create a DSM of difference (DoD) (i.e. negative values indicate elevation lowing or ice loss) which was used to determine the overall height change on the monitored glacial area for each pixel of the model. DoD analysis was performed using the Geomorphic Change Detection (GCD) software (Wheaton, 2015). Both May and

November DSMs had different levels of vertical errors associated (i.e. ± 11 cm and ± 16 cm vertical RMSE respectively); it was necessary to use a threshold value as a minimum level of detection (minLOD). The minLOD value of ± 19.41 cm was determined using the following formula which calculated minLOD threshold as the sum of individual DSM errors in quadrature:

$$\delta(z) = \sqrt{\left(\delta(z)_{DSM_{MAY}}\right)^2 + \left(\delta(z)_{DSM_{NOV}}\right)^2} \qquad \text{(i)}$$

Results were reported as volumetric and aerial changes per-pixel and for the entire monitored area of the Annapurna III glacier for the minLOD threshold value (Table 4).

To improve upon the limitations of DSM differencing, a three-dimensional change calculation was performed by doing point cloud differencing using the Multiscale Model to Model Cloud Compare (M3C2) method (Lague et al., 2013) in the CloudCompare software. M3C2 algorithm first selects a set of points (also called ‘core points’) on which it computes best-fitting normal direction. In the second step, the distance between two point clouds is computed along with a cylinder with a given radius (D/2) projected into the normal direction. The two required user-defined parameters for M3C2 are normal scale *D*, which is used to calculate the surface normal for each point and projection scale *d* over which the cloud to cloud distance calculation is averaged. The optimal values for both of these parameters depends on the properties of the cloud themselves. The normal direction will vary with the value of *D* due to the local roughness of point cloud, and if *D* is too small M3C2 distance can be overestimated. It is recommended that *D* should be > 20-25 times local roughness and *d* should be enough to have more than four points within the cylinder (Lague et al., 2013). Following Bash et. al, (2018), in this study we chose the optimal value of *D* and *d* by performing roughness calculation on the May 2019 point cloud at a variety of scales. The final values for *D* and *d* were 0.62 m and 0.3 m, respectively.

The propagated RMSE calculated as the quadrature of two UAS surveys was used as the registration error in the point cloud differencing analysis. The M3C2 output includes a point cloud containing M3C2 distance, significant change and distance uncertainty. Distance uncertainty is given as the confidence interval, also called Level of Detection (LOD) given as:

$$\mathrm{LOD}_{95\%}\,(d) = \pm 1.96\left(\sqrt{\frac{\sigma_1(d)^2}{n_1} + \frac{\sigma_2(d)^2}{n_2}} + \mathrm{reg}\right)$$

Where σ_1 and σ_2 represent that roughness of individual point cloud in subset of clouds of diameter d and size of n_1 and n_2 and reg is the registration error. The distribution of registration error is expected to be spatially uniform and isotropic (Lague et al., 2013). If the |M3C2 distance|> C95% the significance value is 1 or otherwise 0. The significance values were used to filter and select only the significant M3C2 values on which mean and standard deviation were calculated. The significant M3C2 distance values were analyzed for the entire monitored area of the glacier as well as selected smaller regions of the glacier to better understand the glacier dynamics and associated driving factors.

3. Results and discussion

3.1 GNSS and DSM Accuracy

The co-ordinates of the dGPS base station were positioned with an estimated (vertical+horizontal) error of 0.046 m during May 2019 and error of 0.066 m during the November 2019 campaign. After post-processing the GCPs and check points with Trimble Pathfinder Office, their positional errors were estimated to be under 0.03 m (May 2019) and 0.039 m (Nov 2019). Thus maximum expected positional error for the two surveys was 0.069 m.

The accuracy of the DSMs generated by Pix4D was accessed based on the residuals of the GCPs. The distribution of the GCP residual for May 2019 shows that at the GCP locations, the DSM had accuracy with 0.20 m for both vertical and horizontal directions. For the November 2019 DSM, the errors were within 0.30 m. However, for the majority of the measurements error was less than 0.15 m.

The error statistic provided above tends to overestimate model accuracy. SfM processing in its various stages (i.e. aligning images, DSM generation and Orthorectification) introduces some error. DSM accuracy should therefore be evaluated by comparing survey points not used in model generation (i.e. check points) and comparing DSM difference over the off-glacier terrain area that is expected to experience no vertical change. Comparison of DSM with check points for May 2019 showed a mean difference of -0.0019325 m with a standard deviation of 0.11978 m. For November 2019 DSM, the observed mean difference was -0.0408125 m with a standard deviation of 0.109626 m. Figure 6 shows the histogram of the elevation difference for the off-glacier area outlined in Figure 1 which shows that the average deviation between the two DSM was 0.01 m ± 0.13 m. This result highlights that the point clouds and DSMs used in the following analyses were aligned accurately.

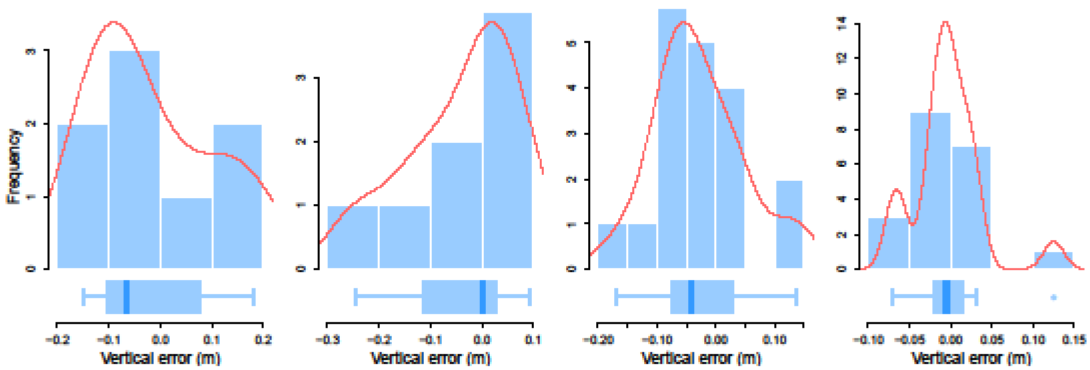

Figure 5: Histograms of differences (errors) between check points and GCP surveyed elevations and DSM elevation for May 2019 and November 2019. (a) May 2019 check points, (b) November 2019 check points, (c) May 2019 GCP and (d) November 2019 GCP.

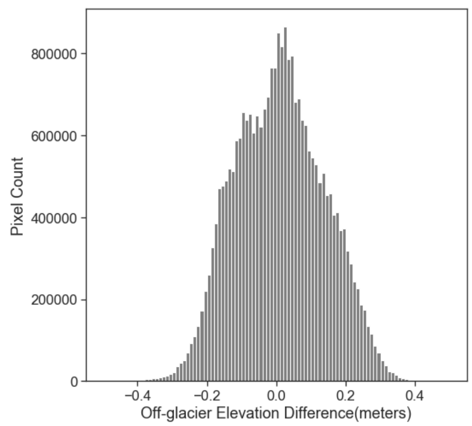

Figure 6: Histogram of elevation differences between May and November 2019 for the off-glacier area shown in Figure 1.

3.2 Measured changes over the compared glaciated area

Results of DSM differencing showed that the pattern in surface elevation changes (loss or gain) was highly heterogeneous across the monitored glacial area. An overall loss of surface elevation was observed (represented by negative change) during the observed ablation season (Figure 7). The mean surface elevation change for the entire monitored area was -0.89 m with a standard deviation of 1.19 m (for ± 19.41 cm LoD). This is equivalent to 255,882 ± 48,681 m^3 of ice loss

(Table 4). The maximum observed down-wasting rate was -11.55 m and the maximum surface raising was +4.2 m. Vast majority (~96%) of the values were within -3.9 m to + 0.87 m (Figure 7.a). The mean surface elevation change observed in this study for Annapurna III glacier is lower than those observed by Immerzeel et al. (2014) for the Lirung glacier (i.e. -1.09 m with a SD of 1.4 m) during roughly the same monitoring months of ablation season.

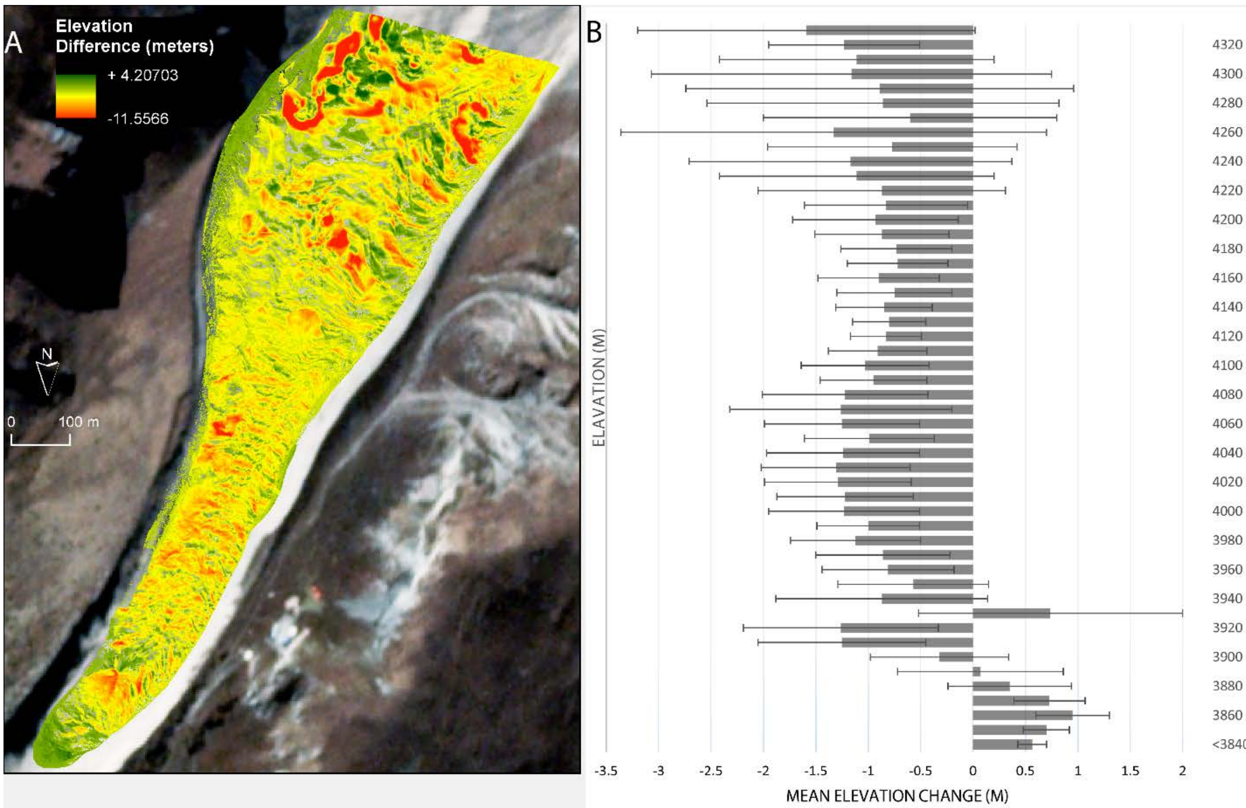

Figure 7: (A) DSM difference derived vertical changes in elevation from May to November 2019 and (B) distribution of changes in elevation calculated by 10 m elevation bands with the gray bars indicating mean change with ± one standard deviation.

Table 4: Changes in elevation and volume between May and November on Annapurna III glacier

	LoD = 0.1941 m
Total Area of Interest (m^2)	348,343
Total Area of Detectable Change (m^2)	288,983
Total Area of Surface Lowering (m^2)	238,006
Total Area of Surface Raising (m^2)	50,977
Total Volume of Surface Lowering (m^3)	289,381 ± 47,601
Total Volume of Surface Raising (m^3)	33,499 ± 10,195
Total Net Volume Difference (m^3)	-255,882 ± 48,681

Percentages by volume:	
Percent Elevation Lowering	90%
Percent Elevation Raising	10%

Figure 7.B shows mean and standard deviation of elevation change as measured within 10 m elevation bands over the glacier measured area, which further highlights nuances into the spatial variation of the distribution of elevation change. Mean elevation change for the highest-altitude band (>4320 m) is the highest at -1.59 m due to the expansion and collapse of ice-cliffs. Variability (standard deviation) in mean elevation change is also found to be higher in the surrounding area (between 4260 m - 4270 m). The mean ice loss pattern does not show a clear elevation dependence as areas with higher mean elevation loss (>4250 m) are followed by a decreasing mean elevation loss (between 4220 m – 4120 m), which is again followed by a higher mean elevation loss bands at the lower elevations (between 3990 m – 4040 m). Interestingly, the lowest elevation areas occupied by the glacier (i.e. glacier snout and adjoin glacier reaches) show a positive rather than negative mass balance with some observed elevation gain. Here a mean elevation increase of 0.48 m (between 3829 and 3880 m) is observed (Figure 7.B).

Throughout the monitored area, zones of elevation decrease were followed by zones of elevation increase. This is likely due to the downslope movement of the glacial ice as the vertical emergence velocity pushes the ice forward. This is also evident from the flow direction of the velocity vectors. The upper reaches of the glacier (area above 4100 m elevation) is in direct contact with the ice fall area with a very steep slope. The mass in the ice-fall region pushes mass in the upper reaches of the monitored area (between 4100 and 4325 m), with a comparatively lesser steep slope, ice is compressed and pushed downslope, resulting in the formation of ice-cliffs and adjacent depressions.

Results obtained from the point cloud differencing (using M3C2 algorithm) showed similar difference in elevation change and spatial distribution. Figure 8.a shows the spatial distribution of 3D cloud-to-cloud difference (where negative value represents elevation loss), and the distribution of M3C2 distance values are also summarized as a histogram in Figure 9. Around 63.3% of points in the resultant point cloud had statistically significant M3C2 distance values. These points with significant M3C2 distance had a mean of -1.34 m and a standard deviation of ±1.32 m. The spatial distribution of M3C2 distance closely matched the DSM differencing results and confirm the spatial distribution of elevation change over the monitored area. Figure 8.b shows if the distance was found to be statistically significant. No significant change was observed for the boulders and debris in the periglacial area, confirming the accurate alignment of the two DSMs.

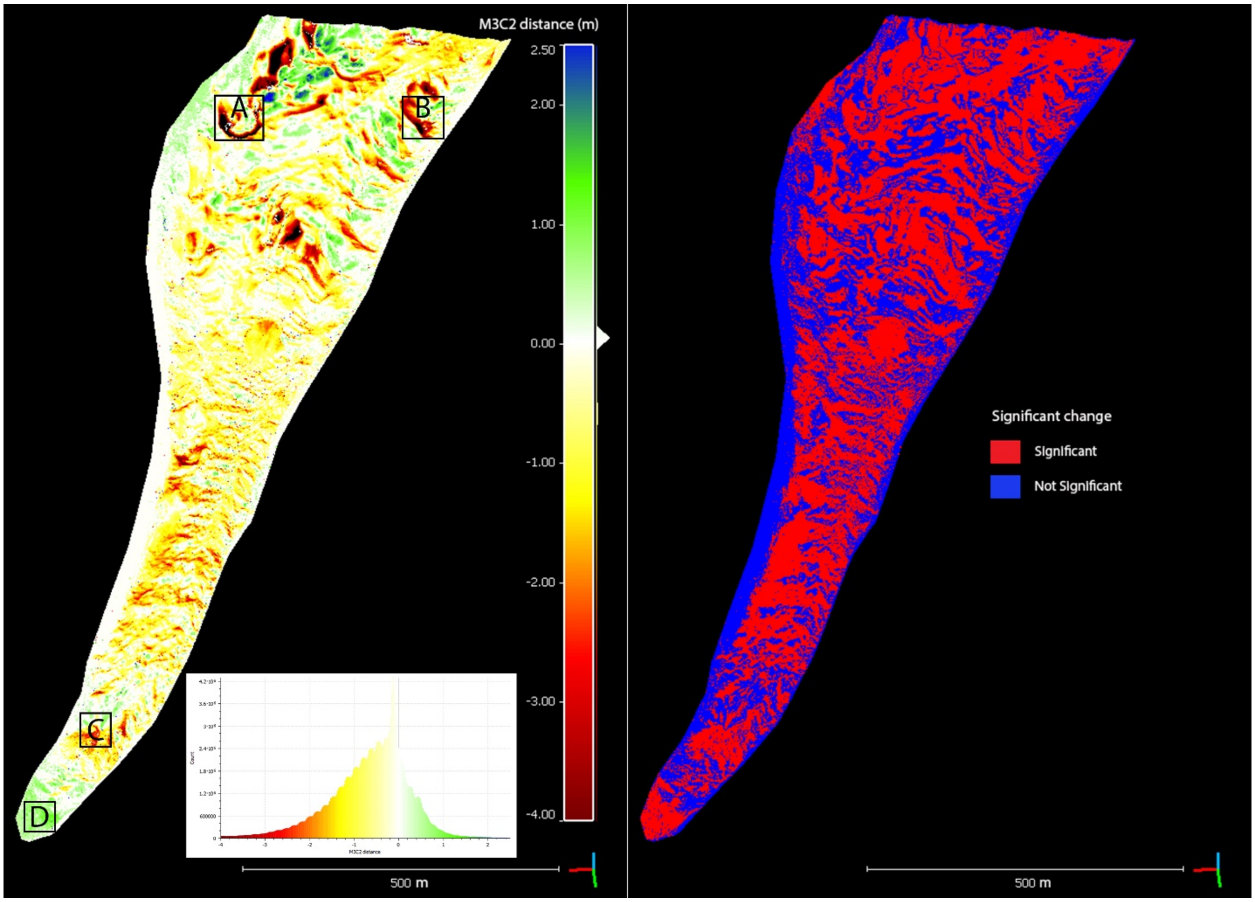

Figure 8: (a) M3C2 algorithm derived distance between two point clouds and (b) significance (95% confidence level) of the estimated change. Four areas of interests marked as boxes A-D in (a) are shown in the next four plots.

3.3 *Interpretation of point cloud differencing results for selected areas*

Previous studies report that glacier surface melt contributes only a small proportion to the mass change of debris-covered glacier, whereas the interplay of englacial voids, supraglacial ponds and cliffs responsible for majority of the mass loss (Brun et al., 2016; Steiner et al., 2015). To examine these interactions, we selected four specific areas on the glacier tongue (highlighted as boxes A, B, C and Din figure 8.a). Results from the analysis of 3-D point cloud differencing for these four areas are shown in detail in figures 9-12.

Both, the largest absolute elevation change (i.e. > 5 m of ice loss) and highest spatial variability in elevation change were observed in the vicinity of ice-cliffs and adjacent areas. Figure 9 shows an example of the movement and expansion of a selected ice-cliff. Here, substantial mass wasting is observed as a large ice-cliff with exposed ice evolved between May and November. Visualization of May point cloud confirmed the existence of supraglacial ponds at the base of the ice-cliff. The 2-D profile (shown in Figure 9e) of a selected transect (transect a-b shown in Figure 9d) revealed that the spatial pattern of mass wasting. The cliff collapse resulted in up to 9 m elevation loss and also led to the development of a glacial moulin between May and November. The ice-cliff expansion and collapse is likely driven by a under cutting of the cliff base due to increased ablation rate due to supraglacial pond contact (Steiner et al., 2015). Several previous studies have emphasized the significant role ice-cliffs play in the overall melt of the debris-covered parts of Himalayan glaciers (Brun et al., 2016; Buri et al., 2016; Sakai et al., 2002). Ice-cliffs, often characterized by steep slopes, are exposed such that it receive higher longwave radiation, which increases their melt rate (Buri et al., 2016; Steiner et al., 2015).

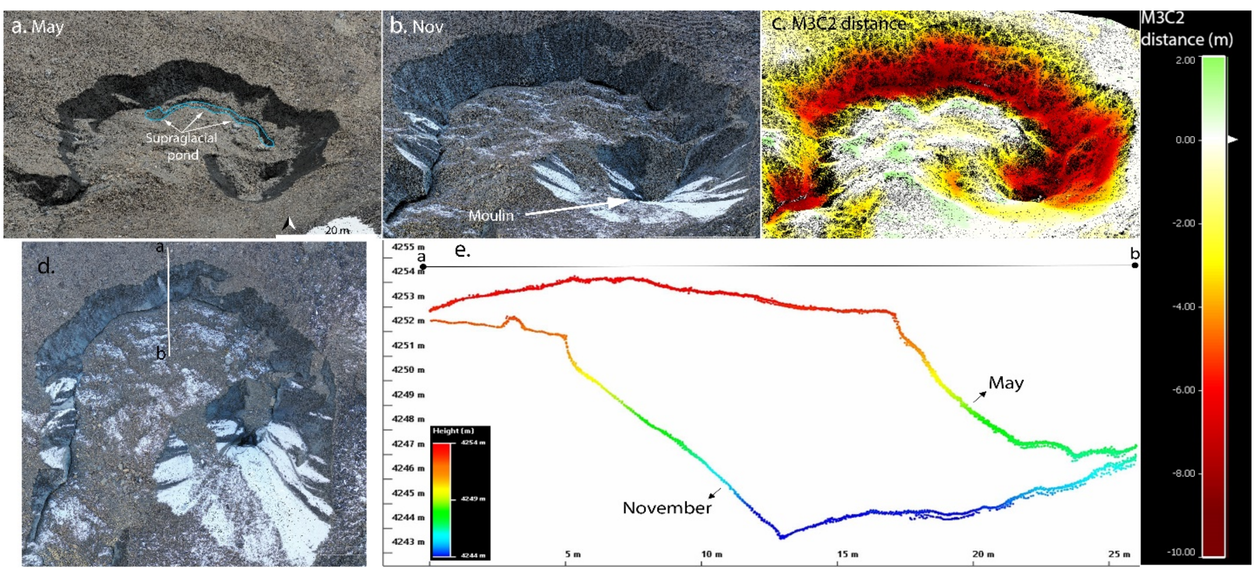

Figure 9: Changes in surface features around a selected ice cliff highlighted in area of interest “A” of Figure 8a. The first and second columns shows the perspective view of densified point clouds of May and November 2019 respectively, the third column shows respective M3C2 distances. The figure in second row shows the nadir view of November point cloud with a

transect. The last panel shows elevational change along the transect by taking all points within 0.1 m on either side of the transect.

Figure 10 shows the same set of results as figure 9 for area of interest “B” shown in figure 8a. This is another area with the existence of the ice-cliffs and supra-glacial pond. This area experienced a slightly lower magnitude of elevation change. In May, the supra glacial pond is ~10 m wide, but gets completely drained in November. Higher amount of mass wasting (−6 m to −10 m elevation loss) was observed at steeper portion of the surrounding ice cliff (left of the pond) compared to less steeper cliffs (−2 to −4 m elevation loss). Large parts of the cliff that were exposed ice in May, were covered with debris and some recent snow in November. The translocation of boulders and the resultant increase in debris cover could be confirmed by visually comparing the May and November point clouds (Figure 10a and 10b).

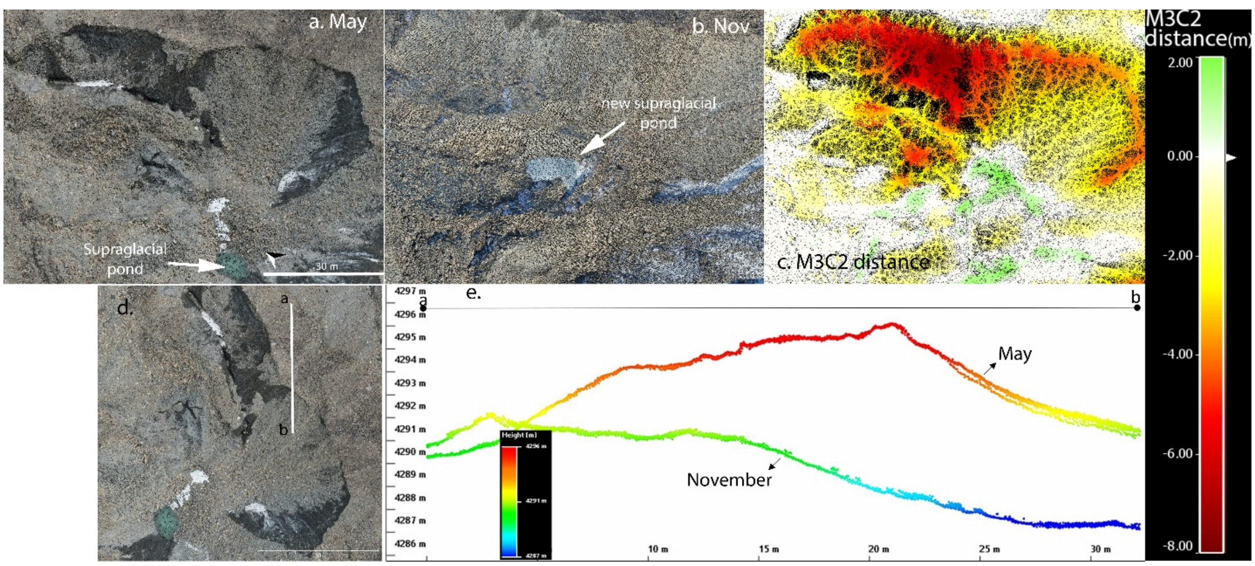

Figure 10. Changes in surface features around a selected ice-cliff highlighted in area of interest “B” shown in figure 8a. Panel descriptions as in figure 9.

Figure 11 shows another dynamic area of englacial depression (possibly a moulin covered by debris), where both mass gain and loss can be observed. The slight mass gain upslope from the depression is most likely due to the slumping and redistribution of debris as well as glacier’s emergence and compressive flow. The dominant mass loss here could be due to sub-debris melt through the process outlined for figure 9.

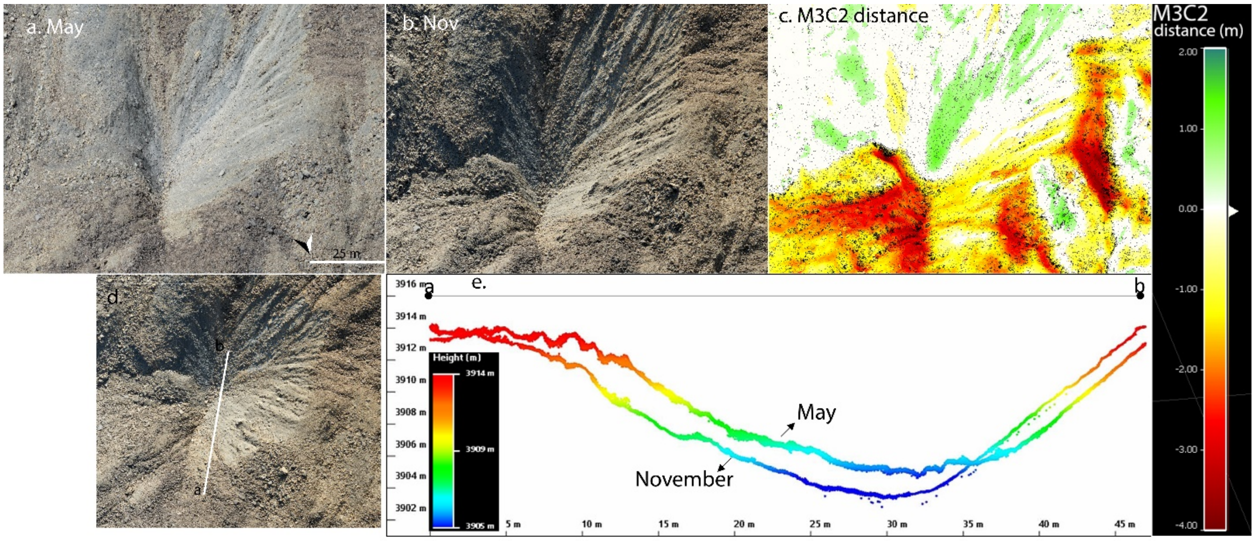

Figure 11. Changes in surface features around the area highlighted in area of interest "C" in figure 8a. Panel descriptions as in figure 9.

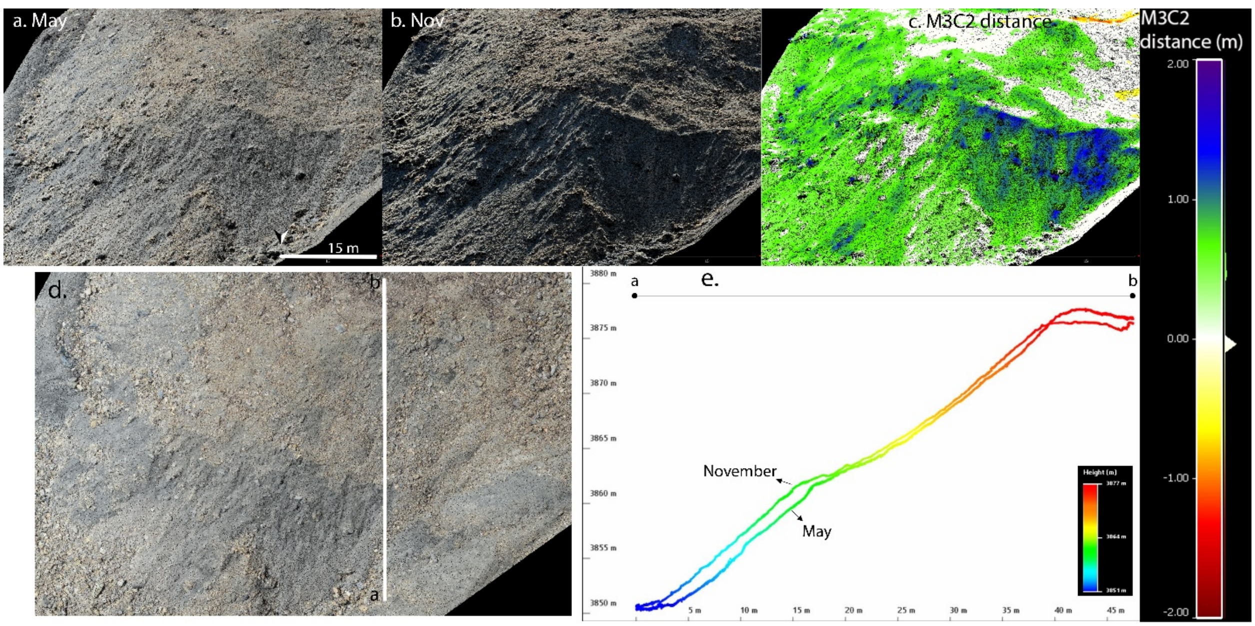

Figure 12. Changes in surface features around the area highlighted in area of interest "D" in figure 8a. Panel descriptions as in figure 9.

Figure 12 shows an area near/just above the glacial snout, which shows moderate elevation gain (+0.5 m to +2.0 m). We hypothesize that the mass gain is due to glacier's emergence velocity (also observed by Watson et al. (2017) on the Khumbu glacier) and well as translocation of debris from upslope areas and the adjoining lateral moraines. Sub-glacial meltwater coming from crevasses, ice-cliffs, supra glacial ponds, and surface melting, tends to increase the basal flow at lower end (see the velocity at point C). The subglacial surface frictional resistance at the snout position does not allow the basal flow at the snout position and beyond (low velocity at point D). As a result, there is compression of the glacier ice and supraglacial debris at the snout position area and hence the slight elevation gain here.

3.*4 Surface velocity*

The velocity of glacier surface ranged from 4.1 m between May and November in the upper part of the on the monitored area of the glacier to completely stationary near the lateral moraines on either sides, and the glacier snout (Figure 11). In general, for the glacier surface velocity distribution, the monitored area could be divided into two parts: the majority of high-velocity area lies above the 4160 m contour, and below this, the glacier area has lower overall velocity. At around 4160 m, there is a sudden break in slope, which generally flattens out at lower elevations. Beyond this broad generalization, however, with localized variations in slope resulted in variations in gradient, and areas with comparatively steeper slopes experienced increased velocity.

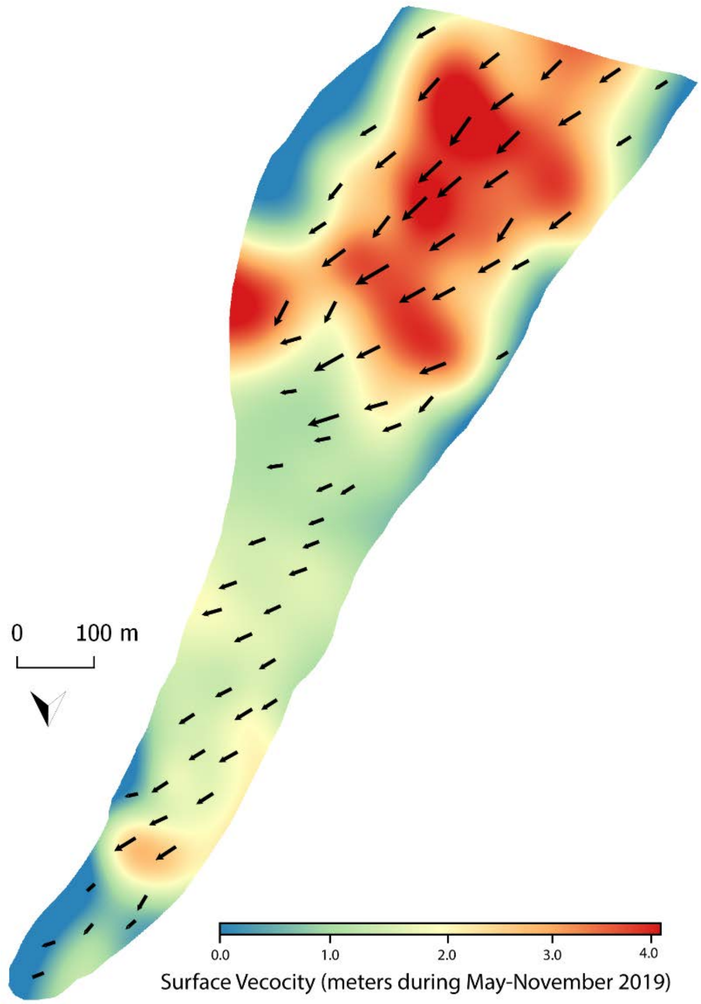

Figure 11: Interpolated glacier surface velocity (shift in position of surface between May and Nov) and their tracks (direction of the shift).

3.5 Comparison to other Himalayan glaciers monitored using UAS

This study presents an application of DSM and 3-D point cloud differencing applied to repeated UAS survey data for detecting topographic change on the lower ablation area of Annapurna III glacier. Unlike Immerzeel et al. (2014) who utilized a fixed-wing UAS platform for data collection, this study utilized a much smaller quadcopter platform. While it is logistically easier to transport, launch and land smaller UAS, it may take higher amount of time and more number of flights to cover comparable area (Bhardwaj et al., 2016). Furthermore, fixed-wing UAS are generally able to carry higher resolution cameras (with global rather than rolling shutter) compared to smaller UAS, this limitation is reducing as high resolution sensors are also being developed and integrated with smaller UAS platforms (Singh and Frazier, 2018).

With an average DSM difference of -0.81 m, the overall melt rate on Annapurna III glacier is lower compared to Lirung glacier of the Himalaya (155 kms east of our site) for which Immerzeel et al. (2014) obtained mean surface elevation change of -1.09 m using UAS derived data. However, the high spatial heterogeneity of melt patterns and surface changes we observed are similar to the ones previously published by Immerzeel et al. (2014). Importantly, there are notable differences: (a) situated on the south facing slope of the Himalaya under monsoonal climatic regime, Lirung glacier receives more than twice the amount of annual precipitation compared to Annapurna III which lies outside the monsoonal climatic regime (Immerzeel et al., 2014) (b) unlike Lirung glacier where areas experienced elevation gain (because of change in flow direction resulting in glacier uplift) in a single zone/elevation band, we observed in Annapurna III areas of elevation gain and loss interspersed throughout the glacier and show more heterogeneous distribution pattern; (c) we observed a contiguous region of elevation gain at lower elevation near the snout of the glacier, which is in contrary to the glacier dynamics in Lirung glacier.

Focusing on four areas of interest, we show various drivers of mass wasting such as ice-cliff collapse, undercutting by adjacent supraglacial pond, burial of exposed ice under debris, and draining of ponds over time. Following M3C2 method the mechanism controlling elevation change can be evaluated in 3-D, understanding the role of specific driver (e.g. undercutting by supraglacial pond) and also reduces the chances of misinterpreting topographic change from debris cover, supraglacial ponds and ice-cliffs that occurs in DSM comparison. However, since the M3C2 method calculates 3-D changes along a normal direction and the alignment of surface normal varies over space. Hence, M3C2 methods is not suitable for calculating volumetric ice loss.

4 Conclusions and future research

This study presented the first UAS photogrammetry based volumetric change results for a trans-Himalayan glacier outside the monsoon climatic regime. Our findings from Annapurna III glacier expands the previously sparse database of UAS based monitoring of debris-covered glaciers in the high mountain Asia. UAS derived 3-D point cloud data provides a more realistic representation of glacial surface area compared to planimetric DSM and improves upon the errors associated with DSM differencing. Point cloud differencing based on M3C2 algorithm was shown to be an effective method to quantify the spatial variability in the magnitude of surface elevation change. Results further our understanding of spatial heterogeneity of mass loss patters on debris-covered glaciers in the Himalaya. The ortho-mosaic of the upper portion of the debris cover tongue, captured only during the November mission, confirmed the presence of a higher density of supraglacial ponds and ice cliffs and ice-falls. Future research benefit by focusing on recollecting UAS data for the entire monitored area and estimate the changes in mass balance for the entire area over an inter-annual scale.

Acknowledgements

The authors thank the Home Ministry, Civil Aviation Authority and the Annapurna Conservation Area Project (ACAP) of Nepal for allowing UAS data collection; ACAP officials, and Tashi Gale for guidance and logistical support in the field and Colin Belby for making the dGPS available. The first author would like to thank Bharat Babu Shrestha, Jackson Radenz, Kyle Zerbian, Aaron Christensen, and David Holmes for participating in data collection missions. The first author was funded through Faculty Research Grant from UW-La Crosse, and students were received the Research and Creativity grant and Travel and Supplies Grant from the College of Science and Health at UW-La Crosse.

References

Bash, E.A., Moorman, B.J., Gunther, A., 2018. Detecting short-term surface melt on an Arctic Glacier using UAV surveys. Remote Sensing, 10(10), 1547.

Bhadwal, S., Groot, A., Balakrishnan, S., Nair, S., Ghosh, S., Lingaraj, G., van Scheltinga, C.T., Bhave, A., Siderius, C., 2013. Adaptation to changing water resource availability in Northern India with respect to Himalayan Glacier retreat and changing monsoons using participatory approaches. Science of the Total Environment, 468, S152-S161.

Bhardwaj, A., Sam, L., Martín-Torres, F.J., Kumar, R., 2016. UAVs as remote sensing platform in glaciology: Present applications and future prospects. Remote sensing of environment, 175, 196-204.

Bishop, M.P., Olsenholler, J.A., Shroder, J.F., Barry, R.G., Raup, B.H., Bush, A.B., Copland, L., Dwyer, J.L., Fountain, A.G., Haeberli, W., 2004. Global Land Ice Measurements from Space (GLIMS): remote sensing and GIS investigations of the Earth's cryosphere. Geocarto International, 19(2), 57-84.

Bolch, T., Pieczonka, T., Benn, D., 2011. Multi-decadal mass loss of glaciers in the Everest area (Nepal Himalaya) derived from stereo imagery. The Cryosphere, 5(2), 349-358.

Brun, F., Buri, P., Miles, E.S., Wagnon, P., Steiner, J., Berthier, E., Ragettli, S., Kraaijenbrink, P., Immerzeel, W.W., Pellicciotti, F., 2016. Quantifying volume loss from ice cliffs on debris-covered

glaciers using high-resolution terrestrial and aerial photogrammetry. Journal of Glaciology, 62(234), 684-695.
Buri, P., Pellicciotti, F., Steiner, J.F., Miles, E.S., Immerzeel, W.W., 2016. A grid-based model of backwasting of supraglacial ice cliffs on debris-covered glaciers. Annals of Glaciology, 57(71), 199-211.
Cogley, J.G., 2011. Present and future states of Himalaya and Karakoram glaciers. Annals of Glaciology, 52(59), 69-73.
DJI, 2019. https://www.dji.com/mavic-2/info.
Dobhal, D., Mehta, M., Srivastava, D., 2013. Influence of debris cover on terminus retreat and mass changes of Chorabari Glacier, Garhwal region, central Himalaya, India. Journal of Glaciology, 59(217), 961-971.
Easy, D.M., 2017. Map Pilot for DJI. Online.
Farinotti, D., Huss, M., Fürst, J.J., Landmann, J., Machguth, H., Maussion, F., Pandit, A., 2019. A consensus estimate for the ice thickness distribution of all glaciers on Earth. Nature Geoscience, 12(3), 168-173.
Fujita, K., Suzuki, R., Nuimura, T., Sakai, A., 2008. Performance of ASTER and SRTM DEMs, and their potential for assessing glacial lakes in the Lunana region, Bhutan Himalaya. Journal of Glaciology, 54(185), 220-228.
Hubbard, B., Glasser, N.F., 2005. Field techniques in glaciology and glacial geomorphology. John Wiley & Sons.
Immerzeel, W., Kraaijenbrink, P., Shea, J., Shrestha, A., Pellicciotti, F., Bierkens, M., De Jong, S., 2014. High-resolution monitoring of Himalayan glacier dynamics using unmanned aerial vehicles. Remote Sensing of Environment, 150, 93-103.
Immerzeel, W.W., Van Beek, L., Konz, M., Shrestha, A., Bierkens, M., 2012. Hydrological response to climate change in a glacierized catchment in the Himalayas. Climatic change, 110(3-4), 721-736.
Immerzeel, W.W., Van Beek, L.P., Bierkens, M.F., 2010. Climate change will affect the Asian water towers. Science, 328(5984), 1382-1385.
James, M.R., Robson, S., Smith, M.W., 2017. 3-D uncertainty-based topographic change detection with structure-from-motion photogrammetry: precision maps for ground control and directly georeferenced surveys. Earth Surface Processes and Landforms, 42(12), 1769-1788.
Kääb, A., Berthier, E., Nuth, C., Gardelle, J., Arnaud, Y., 2012. Contrasting patterns of early twenty-first-century glacier mass change in the Himalayas. Nature, 488(7412), 495-498.
Kaltenborn, B.P., Nellemann, C., Vistnes, I.I., 2010. High mountain glaciers and climate change: challenges to human livelihoods and adaptation. UNEP, GRID-Arendal.
Kansakar, S.R., Hannah, D.M., Gerrard, J., Rees, G., 2004. Spatial pattern in the precipitation regime of Nepal. International Journal of Climatology: A Journal of the Royal Meteorological Society, 24(13), 1645-1659.
Kehrwald, N.M., Thompson, L.G., Tandong, Y., Mosley-Thompson, E., Schotterer, U., Alfimov, V., Beer, J., Eikenberg, J., Davis, M.E., 2008. Mass loss on Himalayan glacier endangers water resources. Geophysical Research Letters, 35(22).
Kirschbaum, D., Watson, C.S., Rounce, D.R., Shugar, D., Kargel, J.S., Haritashya, U.K., Amatya, P., Shean, D., Anderson, E.R., Jo, M., 2019. The State of Remote Sensing Capabilities of Cascading Hazards Over High Mountain Asia. Frontiers in Earth Science, 7, 197.
Lague, D., Brodu, N., Leroux, J., 2013. Accurate 3D comparison of complex topography with terrestrial laser scanner: Application to the Rangitikei canyon (NZ). ISPRS journal of photogrammetry and remote sensing, 82, 10-26.
Lowe, D.G., 1999. Object recognition from local scale-invariant features, Proceedings of the seventh IEEE international conference on computer vision. Ieee, pp. 1150-1157.

Lucieer, A., Jong, S.M.d., Turner, D., 2014. Mapping landslide displacements using Structure from Motion (SfM) and image correlation of multi-temporal UAV photography. Progress in Physical Geography, 38(1), 97-116.
Mishra, N.B., Mainali, K.P., 2017. Greening and browning of the Himalaya: Spatial patterns and the role of climatic change and human drivers. Science of The Total Environment, 587, 326-339.
Mishra, N.B., Mainali, K.P., Shrestha, B.B., Radenz, J., Karki, D., 2018. Species-level vegetation mapping in a Himalayan treeline ecotone using unmanned aerial system (UAS) imagery. ISPRS International Journal of Geo-Information, 7(11), 445.
Oerlemans, J., 2001. Glaciers and climate change. CRC Press.
Paul, F., Bolch, T., Kääb, A., Nagler, T., Nuth, C., Scharrer, K., Shepherd, A., Strozzi, T., Ticconi, F., Bhambri, R., 2015. The glaciers climate change initiative: Methods for creating glacier area, elevation change and velocity products. Remote Sensing of Environment, 162, 408-426.
Pellicciotti, F., Stephan, C., Miles, E., Herreid, S., Immerzeel, W.W., Bolch, T., 2015. Mass-balance changes of the debris-covered glaciers in the Langtang Himal, Nepal, from 1974 to 1999. Journal of Glaciology, 61(226), 373-386.
Pix4D, 2019. Pix4D Documentation.
Ragettli, S., Bolch, T., Pellicciotti, F., 2016. Heterogeneous glacier thinning patterns over the last 40 years in Langtang Himal, Nepal. The Cryosphere.
Rossini, M., Di Mauro, B., Garzonio, R., Baccolo, G., Cavallini, G., Mattavelli, M., De Amicis, M., Colombo, R., 2018. Rapid melting dynamics of an alpine glacier with repeated UAV photogrammetry. Geomorphology, 304, 159-172.
Sakai, A., Nakawo, M., Fujita, K., 2002. Distribution characteristics and energy balance of ice cliffs on debris-covered glaciers, Nepal Himalaya. Arctic, Antarctic, and Alpine Research, 34(1), 12-19.
Scherler, D., Bookhagen, B., Strecker, M.R., 2011. Spatially variable response of Himalayan glaciers to climate change affected by debris cover. Nature geoscience, 4(3), 156-159.
Schickhoff, U., Mal, S., 2020. Current Changes in Alpine Ecosystems of Asia.
Shrestha, A.B., Aryal, R., 2011. Climate change in Nepal and its impact on Himalayan glaciers. Regional Environmental Change, 11(1), 65-77.
Singh, K.K., Frazier, A.E., 2018. A meta-analysis and review of unmanned aircraft system (UAS) imagery for terrestrial applications. International Journal of Remote Sensing, 39(15-16), 5078-5098.
Smith, M., Carrivick, J., Quincey, D., 2016. Structure from motion photogrammetry in physical geography. Progress in Physical Geography, 40(2), 247-275.
Snavely, N., Seitz, S.M., Szeliski, R., 2008. Modeling the world from internet photo collections. International journal of computer vision, 80(2), 189-210.
Steiner, J.F., Pellicciotti, F., Buri, P., Miles, E.S., Immerzeel, W.W., Reid, T.D., 2015. Modelling ice-cliff backwasting on a debris-covered glacier in the Nepalese Himalaya. Journal of Glaciology, 61(229), 889-907.
Sud, R., Mishra, A., Varma, N., Bhadwal, S., 2015. Adaptation policy and practice in densely populated glacier-fed river basins of South Asia: a systematic review. Regional Environmental Change, 15(5), 825-836.
Switzerland, P.D., 2018. Pix4Dmapper Pro-Educational. Version, 4, 25.
Triggs, B., McLauchlan, P.F., Hartley, R.I., Fitzgibbon, A.W., 1999. Bundle adjustment—a modern synthesis, International workshop on vision algorithms. Springer, pp. 298-372.
Trimble, 2000. GPS Pathfinder Office Getting Started Guide. Trimble Navigation Limited Sunnyvale, California.
Watson, C.S., Quincey, D.J., Smith, M.W., Carrivick, J.L., Rowan, A.V., James, M.R., 2017. Quantifying ice cliff evolution with multi-temporal point clouds on the debris-covered Khumbu Glacier, Nepal. Journal of Glaciology, 63(241), 823-837.

Wheaton, J., 2015. Geomorphic Change Detection Software. Utah State University.
Wigmore, O., Mark, B., 2017. Monitoring tropical debris-covered glacier dynamics from high-resolution unmanned aerial vehicle photogrammetry, Cordillera Blanca, Peru. The Cryosphere, 11(6).
Xu, J., Grumbine, R.E., Shrestha, A., Eriksson, M., Yang, X., Wang, Y., Wilkes, A., 2009. The melting Himalayas: cascading effects of climate change on water, biodiversity, and livelihoods. Conservation Biology, 23(3), 520-530.